Damage mechanisms in short glass fibre reinforced thermoplastic during *in situ* microtomography tensile tests

H. Rolland [a], N. Saintier [a,*], G. Robert [b]

[a] *I2M, Arts et Métiers ParisTech, Esplanade des Arts et Métiers 33405 Talence, France*
[b] *Solvay Engineering Plastics, Avenue Ramboz, BP 64, 69192 Saint-Fons, France*

A B S T R A C T

Micromechanical modelling of short fibre reinforced thermoplastics requires identification of damage mechanisms and their kinetics as a function of their microstructure. A compact tensile machine has been designed to observe damage mechanisms during *in situ* microtomography tensile tests. 3D pictures of the gage length are presented at different levels of damage, from the initial state to the failure of the specimen. Fibre failure, damage at fibre ends, debonding and damage growth in the matrix have been identified as damage mechanisms for these materials. Vicinity between crossing fibres has been pointed out as microstructural configurations driving the damage mechanisms. An analysis of the damage evolution (density, morphology and orientation) allows to establish a macroscopic failure scenario, consistent with microscopic observations.

Keywords:
In situ microtomography
A. Thermoplastic resin
C. Damage mechanics
E. Injection moulding

1. Introduction

With increasing constraints of weight reduction in industrial fields, mechanical properties are now considered regarding material density. This trend ranks the short glass fibre polyamide 6,6 among very promising materials, whence emerges the need to describe its behaviour. The complexity mainly comes from the microstructure of the material: the injection process, perfectly suited for high productivity and complex shapes, induces heterogeneous distribution and orientation of fibres [1,2]. Furthermore, the mechanical performance of these composites results from a combination of fibre and matrix properties and the ability to transfer stresses across the fibre−matrix interface as indicated by Thomason's works [3,4]. Micromechanical approach is an efficient way to model short fibre reinforced thermoplastics behaviour. This approach requires damage mechanisms knowledge and strain and stress thresholds values. Current experimental challenges consist in observing and localise damage initiation and its development in the reinforced polymer at the appropriate scales, i.e. micro scale. Despite significant works, there still is a lack of data about the link between microstructure and damage mechanisms. Reference work in the field results from combining scanning electron microscopy (SEM) observations and acoustic emissions analysis: a description of damage chronology has been made by Horst [5] and Sato [6,7] for tensile stresses. They highlight main damage mechanisms, in a localized region subjected to stress concentration: 1) Initiation of interfacial microfailure at the fibre ends. 2) Propagation of interfacial microfailure along fibre sides. 3) Occurrence of plastic deformation band in matrix region. 4) Crack opening and slow crack propagation. 5) Fast crack propagation. SEM provide high resolution observations but only surface information that may not be representative of mechanisms proportions and kinetics in the bulk of the specimen. In order to reach the exact nature of bulk damage mechanisms (i.e. damage location with respect to 3D microstructure), microtomography is probably the most efficient tool [8,9]. The development of this technology over the past ten years now allows to reach resolutions (in the micron range) and acquisition times suitable for *in situ* tensile tests for 3D damage evaluation in reinforced thermoplastics [10]. In this paper *in situ* synchrotron X-ray microtomography tensile tests were performed in order to evaluate the evolution of damage in the gage length of a tensile specimen. This method was used (as detailed in Section 2) to describe qualitatively (Sections 3.2 and 3.3) and quantitatively (Section 3.4) the damage mechanisms according to the local microstructure configurations. These results allow to establish a damage scenario (exposed in Section 3.5) for short glass fibre reinforced polyamide under monotonic loading.

* Corresponding author.
E-mail address: nicolas.saintier@ensam.eu (N. Saintier).

http://dx.doi.org/10.1016/
j.compositesb.2015.12.021

2. Material and methods

This work is the result of a combination between mechanical tests management and X-ray microtomographic observations. Such an experimental set up is called *in situ* because the measure of damage is made during the test. Following paragraphs indicate parameters used for this experimental procedure.

2.1. Microtomography

X-ray computed microtomography is an observation technique based on the acquisition of a large number of X-ray radiographs obtained for different angular positions of the sample with respect to the beam. These sets of X-ray radiographs are arranged with a standard filtered back projection reconstruction algorithm to obtain the three dimensional distribution of the linear X-ray attenuation coefficient μ within the sample. This analytical method is faster than algebraic ones, but requires a complete set of radiographs during the rotation and cannot deal with missing views [11]. The elementary unit of the resulting 3D picture, is called a voxel (*volumetric pixel*).

Experiments presented in this work were performed on ID19 beamline at the European Synchrotron Radiation Facility (Grenoble, France). A monochromatic X-ray beam was used, with a 194.77 mA intensity. One of the difficulties of this experimental work is to optimize these parameters to manage both quality of the signal and sample stability. Exposure time is there a key element: in one hand, it has to be short enough to limit viscoelastic relaxation of the sample. In other hand, this time has to be sufficient to allow a satisfying signal with a relatively low photon energy (19 keV in this study), to prevent material degradation. After different tested configurations, an exposure time of 0.2 s has been chosen, with a reduced number of radiographs (2000). These radiographs are received by a Fast Readout Low Noise (FReLoN) 14-bit CCD camera with 2048 $\times$ 2048 pixels, during rotation of the machine over 180° along vertical axis. This experimental set-up was optimized to obtain a voxel edge size of 0.7 μm. The acquisition of a complete scan lasts about 9 min.

2.2. Compact tensile machine

A displacement controlled and force measuring machine was developed. One of the key factors regarding 3D image quality is the distance between the specimen and the CCD sensor. The tensile machine was designed to minimize that distance (less than 30 mm). The loading ring was made of 2 mm thickness PMMA tube in order to reduce additional attenuation by the experimental set-up. The machine was directly mounted on the rotating stage of the beam line as shown in Fig. 1. A load cell was specifically designed and an optical camera was synchronised in order to capture the specimen deformation at different loading stages. The machine capacity is 2*kN* and the displacement is controlled with 0.35 mm increments.

2.3. Specimen

The studied material is Technyl® A218V30, a commercial grade of polyamide 6,6 reinforced by 30 wt% of short glass fibre supplied by Solvay Engineering Plastics-France. In addition to an intricate behaviour, the matrix of this material shows sensitivity to its conditioning. Indeed, effect of water content on polyamide 6,6 mechanical properties has been demonstrated [12–14]. For this reason, the water content of all specimens was controlled and fixed at 50% of relative humidity (RH50). Considering the short duration of each experiment, the water content was considered as constant between the beginning and the end of the tensile tests.

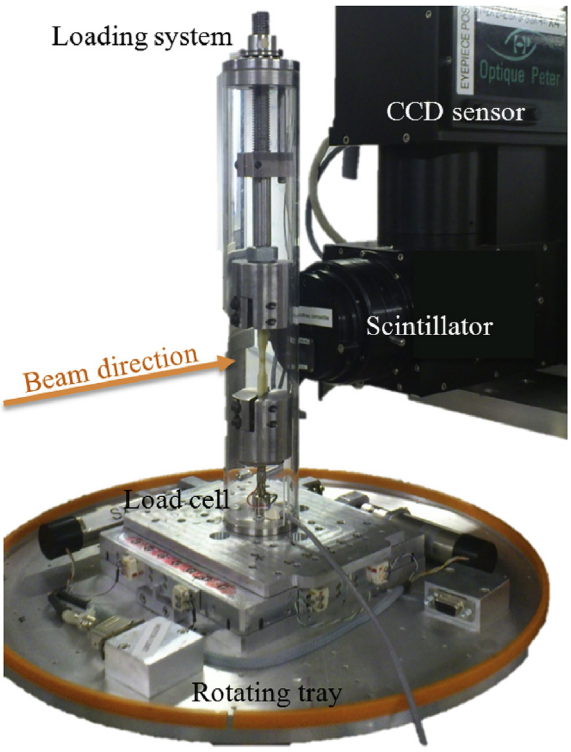

Fig. 1. Compact tensile machine set up for *in situ* testing at ESRF ID19.

The geometry of the specimen was designed to accommodate the constrains of the experimental set-up. Indeed, 3D X-ray microtomography only allows to observe relatively small volumes, depending on resolution and sensor size. The synchrotron experimental set-up described in the previous section allows to obtain a cylindrical observed zone of 1.4 mm diameter and 1.4 mm height (2048 pixels $\times$ 0.7 μm resolution). The gage length was set so that the stress state in the observed volume was homogeneous and a square section was chosen to improve microtomography quality (compared to a rectangular section). Taking into account these elements, the geometry of the specimen was chosen as presented in Fig. 2 obtained by water-cut from injected plates. This geometry allows to obtain similar tensile tests results as on full scale normalised tensile specimens (gage length of 3.24 mm $\times$ 14.1 mm $\times$ 20.0 mm) obtained by the same process.

Fig. 2 also shows the fibres arrangement in the initial obtained volume. This microstructure is composed of more than 25,000 fibres and several thousands of damage markers at each stage of the tensile *in situ* experiment, so that the representativeness of the obtained data is ensured. Fibres have a constant diameter of 10.9 μm. Their length is distributed between 20 and 800 μm, as seen in Fig. 3, with a mean length of 234.3 μm and a standard deviation of 152.1 μm.

The orientation of fibres is heterogeneous in the thickness of the specimen: a core–shell–skin structure is induced by the injection process used to form rectangular plates [15]. This structure, typically observed for injection moulded short fibres reinforced thermoplastics, is characterised by three distinguishable layers: core, shell, skin, as illustrated in Fig. 4. The skin layer is due to the thermal shock between the injected material and the mould walls. Fibres are frozen in their position and orientation forming a 50 μm

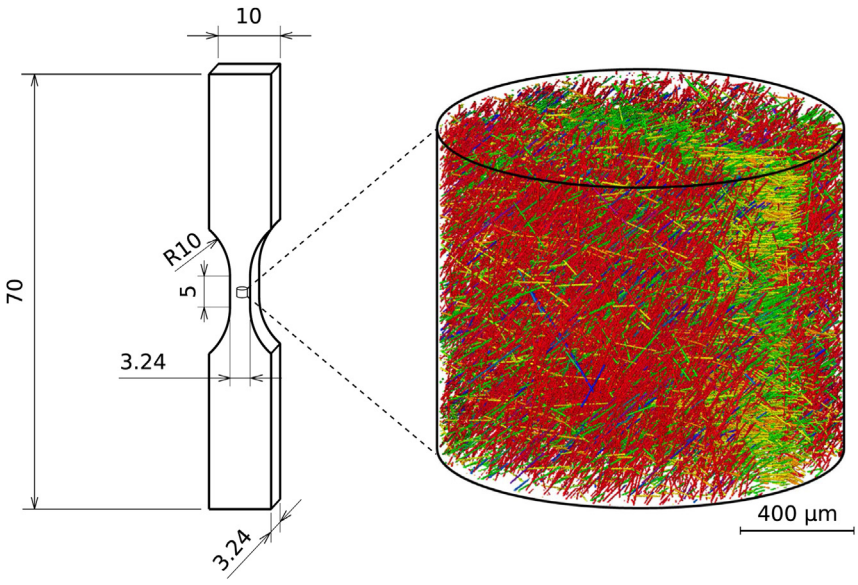

Fig. 2. Specimen geometry for *in situ* tensile testing and fibres of a global 3D picture.

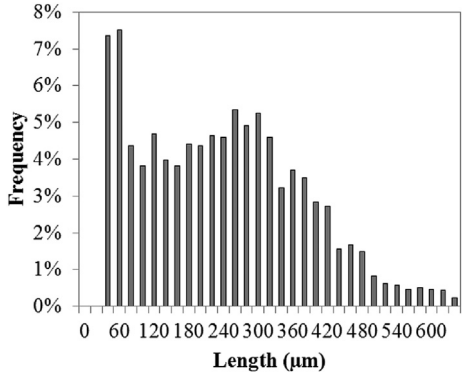

Fig. 3. Fibre length distribution.

thick layer of randomly oriented fibres. The shell layer is the largest with a thickness of 1.4 mm. In this layer, a shear stress of the material flow orientates fibres in the mould flow direction (MFD). The core layer is 300 µm thick in the centre of the specimen. Contrary to the shell, fibres are there perpendicular to the MFD. This orientation is due to an extensional flow during the injection process. An evaluation of the first component of the orientation tensor through the thickness, obtained from fibres orientation distribution is also presented in Fig. 4. The structure induces a rotation of the axes of orthotropy in the thickness of the specimen. So, each specimen has to be considered as a structure with variable mechanical properties in the thickness.

The observed zone by microtomography is centred in on the core as shown in Fig. 2, so each 3D picture contains the core (300 µm), surrounded by two parts of 550 µm thick from the shell. Thus, it is possible to compare fibre orientation distribution in the core and in the shell of the studied specimens, as presented in Fig. 5. Fibres density in the core is slightly higher than in the shell and the shell fibres are mostly oriented toward 45° whereas core fibres have a scattered orientation centered on 63°. For the study, a 45° sampling orientation with respect to the injection direction has been chosen, in order to maximize the symmetry of the microstructure with respect to the loading direction and such limit the mechanical properties evolution in the thickness.

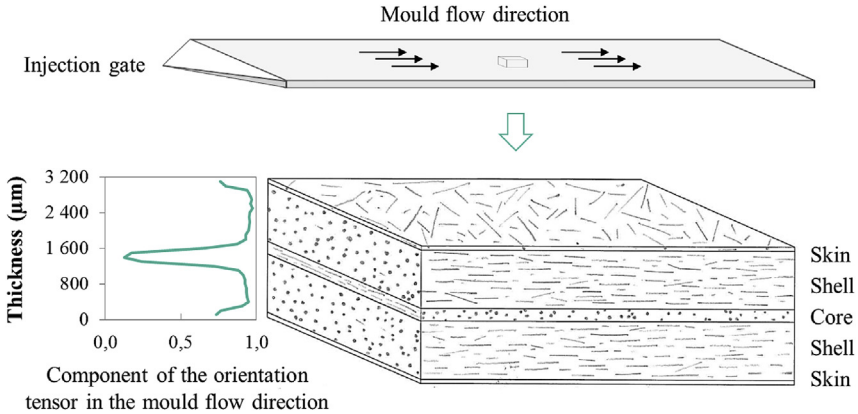

Fig. 4. Core–shell–skin structure in the thickness of the specimen and its influence on the orientation tensor.

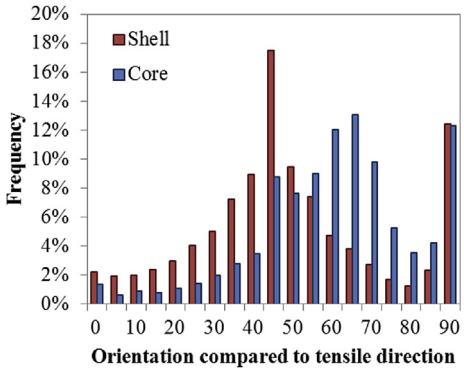

Fig. 5. Fibre orientation distribution with core–shell distinction.

2.4. 3D pictures processing

2.4.1. Thresholds choice on grey levels

Each voxel (voxel edge size = 0.7 μm) forming the 3D picture is defined by a position and a grey level which corresponds to the density of the represented matter. In our case, the grey intensity of the voxel indicates if it belongs to fibre, matrix or damage marker phases. Thus, the first choice to process the image is to determine thresholds on grey levels to distinguish the different phases of the material. Number of voxels for each one of the 65,536 grey levels is presented in the histogram of Fig. 6.

As seen in this figure, the number of voxels whom grey levels under 28,000 is growing during the experiment. From this evolution is deduced the maximal grey level for voxels representing damage markers. The choice for the grey threshold defining the fibre phase is motivated by direct visual determination on the 3D images. It is of clear evidence that the choice of those thresholds has an influence on the observed results. A sensitivity analyses has still to be performed. When these thresholds have been applied, only fibres and damage markers are kept: fibres are seen in blue, damage markers in red and matrix is transparent. This picture treatment has been applied for all illustrations from microtomography in this work.

2.4.2. Used treatments

Using these data from X-ray microtomography, it is possible to observe fibres and damage markers. For further information on them, it is first necessary to identify each object as a system of voxels side by side, of a same phase (damage marker, fibre or matrix). When fibres and damage markers are tailed, by the threshold function and objects separation, it is then possible to obtain coordinates, dimensions, aspect ratio, volume, orientation, for each one. Obviously, quality of these data depends on facility to distinguish phases. In order to improve phases separation, different picture treatments are possible, depending on phases shapes, their volumetric fractions and the difference between their density. Here, damage markers have been analysed directly after the threshold step contrary to fibres, for which it is necessary to apply a sequence of filters (opening, erosion, separation and dilatation) in order to reach the most accurate description of this phase. All these treatments have been applied through Avizo Fire software.

3. Results

3.1. Tensile test results

Results presented here, have been obtained from observations on a 45° extracted specimen, conditioned at 50% of relative humidity. With monitored displacement and load during the test, strain and stress levels for each scan have been determined as indicated in Table 1.

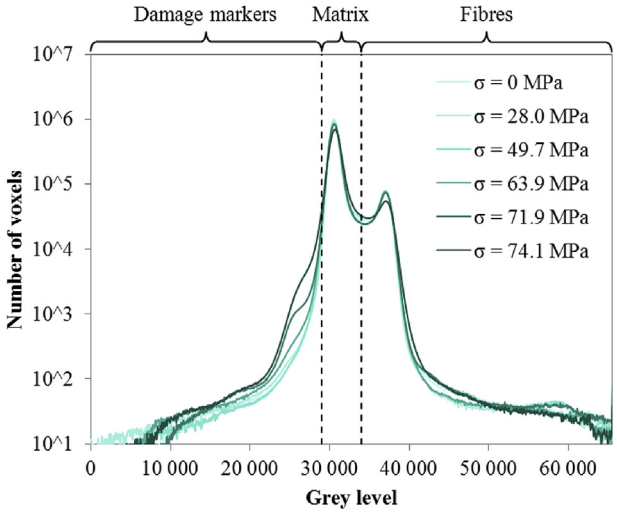

Fig. 6. Number of voxels per grey level at different stress levels.

3.2. Damage mechanisms observations at the micro scale

Four major mechanisms have been identified, strongly dependent on the local 3D microstructure configuration: damage at fibre ends, fibre failure, debonding and damage growth in the matrix. They are illustrated here at the microstructural scale, through four typical damage configurations observed in the specimen gage length at different stages of the tensile test. Their quantitative analysis is presented in Section 3.4.

3.2.1. Damage at fibre ends

Fig. 7 illustrates the evolution of damage at fibre ends. The damage initiates at a macroscopic stress between $\sigma_2 = 28.0$ MPa and $\sigma_3 = 49.7$ MPa. At this stage, the damage marker thickness is about 1 voxel, that corresponds to the minimum detectable element. The damage appears in the form of a penny shape damage marker with a diameter close to the diameter of the fibre.

Two main reasons can explain this damage process. First, as previously mentioned in the literature [16,17] and described in Ref. [18], fibre ends exhibit poor fibre-matrix adhesion properties since sizing is not applied to fibre ends. Indeed, fibres are cut after sizing and additional fibre failure arises during the extrusion process. The second reason is the fibre geometry: fibre ends act as stress concentrators. As the stress increases, the damage marker grows mostly in the direction of the fibre. Two mechanisms can be involved in the damage marker growth: damage growth in the matrix or fibre-matrix debonding along the fibre, inducing larger deformation in the surrounding matrix (pull-out like phenomena). By observing the respective displacement of fibres, the cylindrical shape of the damage marker and by drawing the initial location of the fibre on the final image, it is of clear evidence that the second process is predominant. The debonding cannot be observed after

Table 1
Strain and stress levels for each scan of the tensile test.

Scan number	1	2	3	4	5	6
ε (%)	0	1.1	2.1	3.2	4.2	5.3
σ (MPa)	0	28.0	49.7	63.9	71.9	74.1

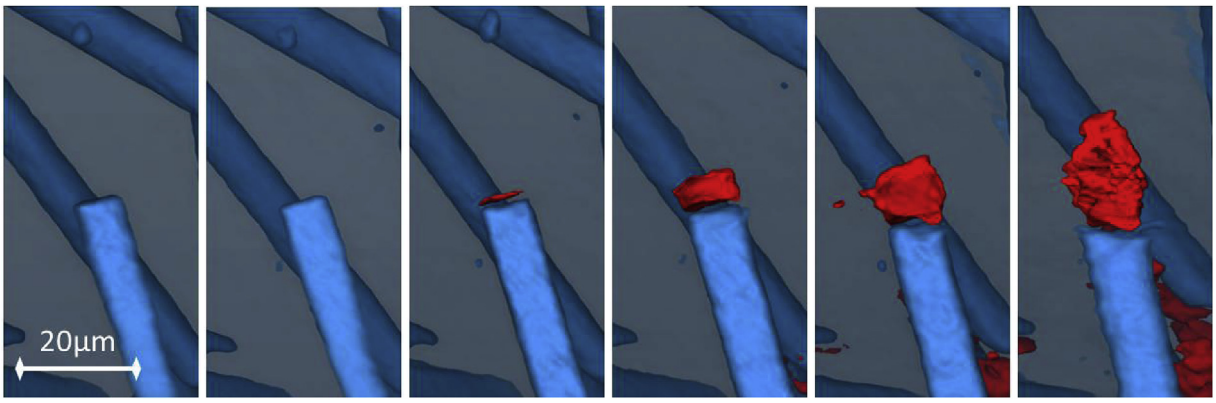

(a) $\varepsilon_1 = 0,0\%$ $\sigma_1 = 0.0$ MPa | (b) $\varepsilon_2 = 1.1\%$ $\sigma_2 = 28.0$ MPa | (c) $\varepsilon_3 = 2.1\%$ $\sigma_3 = 49.7$ MPa | (d) $\varepsilon_4 = 3.2\%$ $\sigma_4 = 63.9$ MPa | (e) $\varepsilon_5 = 4.2\%$ $\sigma_5 = 71.6$ MPa | (f) $\varepsilon_6 = 5.3\%$ $\sigma_6 = 74.1$ MPa

Fig. 7. Growing damage during the tensile test at the end of a fibre (tensile direction is vertical).

image segmentation since this configuration corresponds to a mode II that does not induce significant opening of the resulting defect at RH50. For the same reason, the debonding length cannot be evaluated by direct observation.

On the last stage (Fig. 7(f)) the shape of the damage markers tends to turn into a more spherical and irregular shape that suggests a change in the damage growth mechanism. The growth by pull-out and gliding at the interface turns into damage growth in the bulk of the polymer matrix. This point will be further discussed in the following (paragraph 3.2.4). These observations confirm the pioneer work of Sato [7] and statistical analyses will provide more quantitative details on the extent of this damage process in the volume (see Section 3.4).

3.2.2. *Debonding*

As previously described in the literature [5–7], cohesive properties of the matrix very near to the fibre-matrix interface are essential. Microtomographic observations inform that debonding along fibre sides is not consistently introduced by debonding at fibre ends (as visible in Fig. 8). This mechanism rather seems to depend on local configuration around the fibre and not only on its orientation. Indeed, debonding along fibre sides not only occurs when fibre is oriented transversely to macroscopic stress direction, but mostly when fibre is closely surrounded by fibres with different orientations. The location of this mechanism initiation can be a sign of local stress concentration probably induced by local high confinement of the polymer matrix and short fibre–fibre distance stress field interaction. Also, this mechanism is activated and detected late in the test: it is initiated after the fifth step $\sigma_5 = 71.6$ MPa. The interfacial defect then propagates quickly along a fibre or close to it, inducing a growth partially dependent on fibre orientation.

3.2.3. *Fibre failure*

Fig. 9 illustrates a typical fibre failure mode that has been observed to a large extent in the volume of the material. Two different modes of fibre failure are observed: a transverse mode when the fibre can globally be considered as aligned with the main tensile direction and a longitudinal mode (less frequent, see Fig. 10) when the fibre axis is transverse to the loading direction. Also, fibre failure can occur at different locations on a single fibre. Once the fibre failure occurs, two new fibre ends appears and damage evolves as previously described at original fibre ends. This damage mode was not described previously in the literature as a dominant damage mechanism while largely detected in observations of this study (see results in Section 3.4 and Fig. 17(a)). It can be explained by the surface nature of previously published observations that did not give access to this mechanism developed in the volume of the material. In addition, it is observed that fibre failure occurs at particular locations along the fibre: at points where the fibre crosses other fibres as shown in Fig. 9(f). These locations probably correspond to stress concentration zones along the fibre. As a matter of fact, this mechanism seems to contribute to the failure of the specimen and consequently cannot be longer ignored for two main reasons: as indicated previously, ends of fibre are disposed to damage initiation and each fibre failure creates two new sites for damage initiation. Secondly, because points of failure are weak points: they are the results of local overstress, due to vicinity between two non-parallel fibres. The combination of these two aspects drives these points to be particularly propitious to damage initiation and propagation.

The interest is then to have a better understanding of what happens leading to the failure of a fibre in the material. First, stress values, before and after the failure of the fibre illustrated in Fig. 11, have been identified at the macroscopic scale. Thanks to homogenisation computation, it is possible to have a first estimation of the stress at the micro scale. The Mori-Tanaka's homogenisation scheme [19] has been used considering an ellipsoidal approximation for fibre geometry. The obtained values for the stress in the fibre phase are $\sigma_{MT}^{local} = 168.0$ MPa before fibre failure and $\sigma_{MT}^{local} = 291.1$ MPa after fibre failure, illustrated in Fig. 11(a) and (b). These stress values are far beyond the 2030 MPa reported for E glass fibre tensile ultimate stress [20].

Post mortem SEM observations of fracture surfaces reveal that many fibres exhibits a fracture surface with two zones of different roughness, as shown in Fig. 12(a). The first one (noted A in Fig. 12(a)) consists of smooth surface, associated to a low energy crack propagation, while the second zone (noted B in Fig. 12(a)) reveals a higher roughness. That is considered to correspond to the fibre final failure during the tensile test. The first zone is considered as an initial defect existing in the fibre before the test. In accordance with these observations, a model [21] based on fibres with prior defects has been used to evaluate the local stress required to reach fibre failure.

The measures on SEM pictures have been taken following geometrical description proposed in Fig. 12(b).

The formulation of the stress intensity factor proposed by Astiz [22] in the case of a cylindrical elastic body with a semi-elliptical crack is used. The stress intensity factor for this geometry is given by:

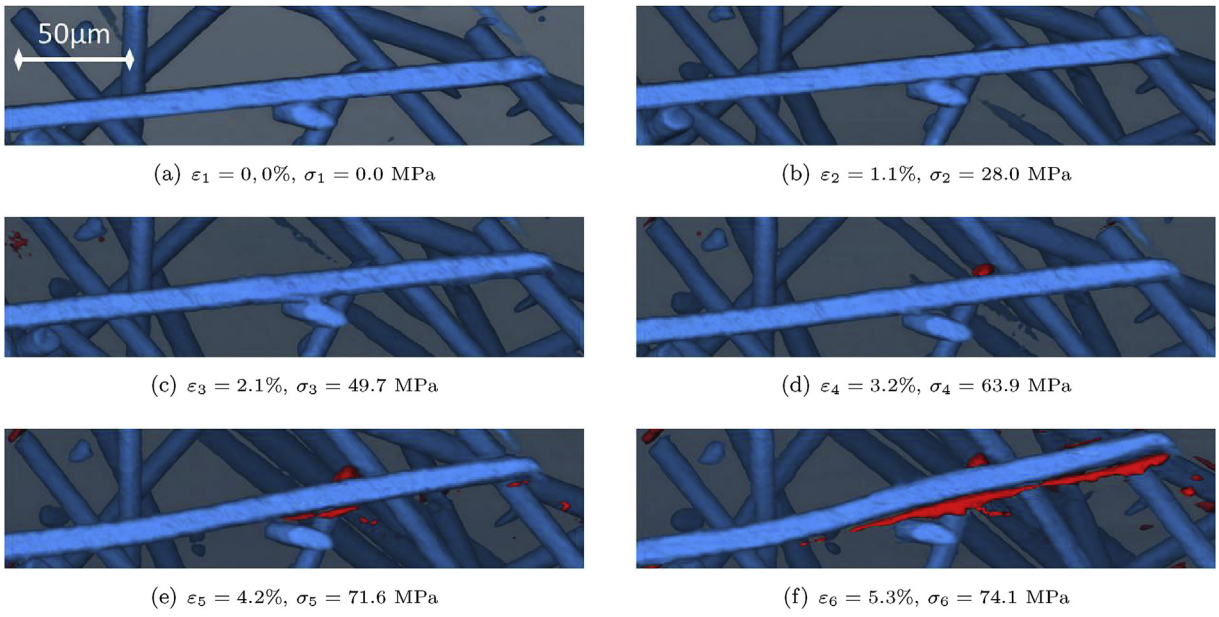

(a) $\varepsilon_1 = 0,0\%$, $\sigma_1 = 0.0$ MPa (b) $\varepsilon_2 = 1.1\%$, $\sigma_2 = 28.0$ MPa

(c) $\varepsilon_3 = 2.1\%$, $\sigma_3 = 49.7$ MPa (d) $\varepsilon_4 = 3.2\%$, $\sigma_4 = 63.9$ MPa

(e) $\varepsilon_5 = 4.2\%$, $\sigma_5 = 71.6$ MPa (f) $\varepsilon_6 = 5.3\%$, $\sigma_6 = 74.1$ MPa

Fig. 8. Debonding at the fibre-matrix interface between two close fibres with different orientations, where confinement is maximum (tensile direction is vertical).

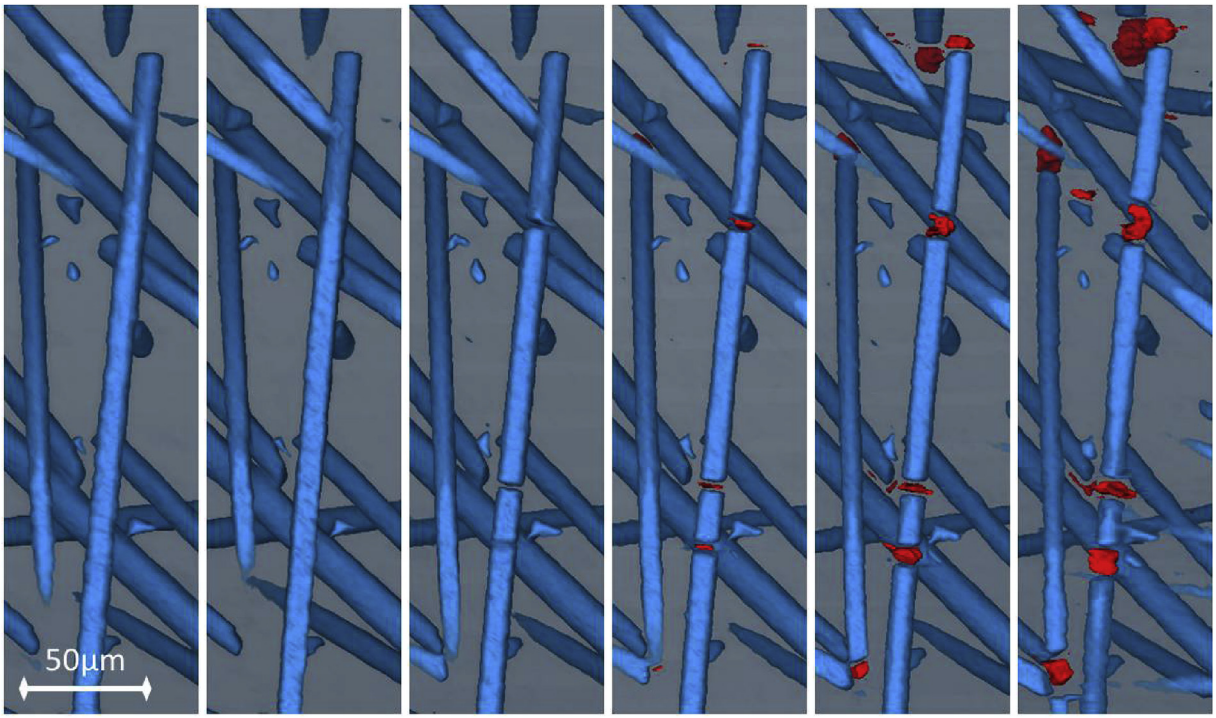

(a) $\varepsilon_1 = 0,0\%$ $\sigma_1 = 0.0$ MPa | (b) $\varepsilon_2 = 1.1\%$ $\sigma_2 = 28.0$ MPa | (c) $\varepsilon_3 = 2.1\%$ $\sigma_3 = 49.7$ MPa | (d) $\varepsilon_4 = 3.2\%$ $\sigma_4 = 63.9$ MPa | (e) $\varepsilon_5 = 4.2\%$ $\sigma_5 = 71.6$ MPa | (f) $\varepsilon_6 = 5.3\%$ $\sigma_6 = 74.1$ MPa

Fig. 9. Example of a fibre failure under monotonic tensile loading (tensile direction is vertical).

$$K_1 = Y\left(\frac{a}{D}, \frac{a}{b}\right)\sigma\sqrt{\pi a} \tag{1}$$

with

$$Y\left(\frac{a}{D}, \frac{a}{b}\right) = \sum_{i=0, i\neq 1}^{4} \sum_{j=0}^{3} C_{ij} \left(\frac{a}{D}\right)^i \left(\frac{a}{b}\right)^j \tag{2}$$

where C_{ij} are the coefficients defined in Table 2 (obtained numerically in Astiz [22]). The crack shape is defined by means of the lengths a and b, respectively representing the crack depth (minor axis of the ellipse) and the major axis. D is the diameter of the cylindrical fibre and F is the axial load applied.

In that case, the stress intensity factor is evaluated between 0.294 MPa.$m^{1/2}$ and 0.51 MPa.$m^{1/2}$ as indicated in the diagram of Fig. 13. These values are lower than usual K_{1C} factor for E-glass

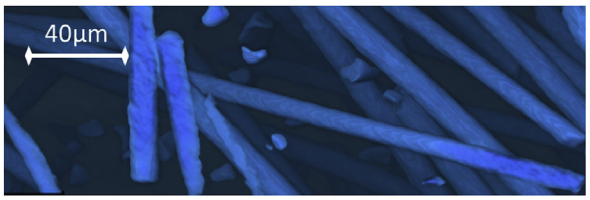

(a) $\varepsilon_1 = 0,0\%$, $\sigma_1 = 0.0$ MPa

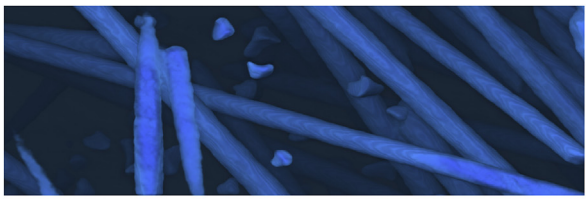

(b) $\varepsilon_2 = 1.1\%$, $\sigma_2 = 28.0$ MPa

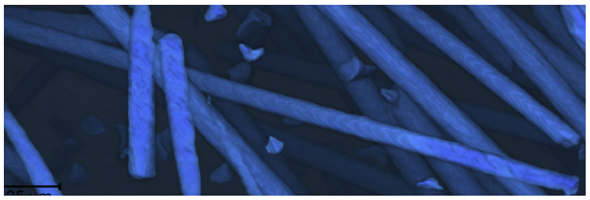

(c) $\varepsilon_3 = 2.1\%$, $\sigma_3 = 49.7$ MPa

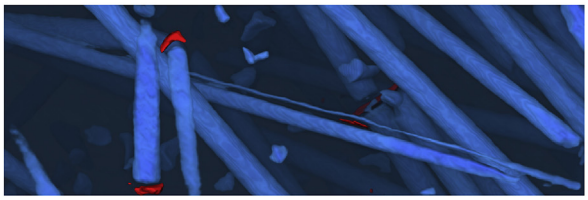

(d) $\varepsilon_4 = 3.2\%$, $\sigma_4 = 63.9$ MPa

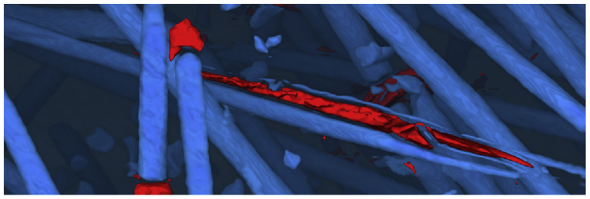

(e) $\varepsilon_5 = 4.2\%$, $\sigma_5 = 71.6$ MPa

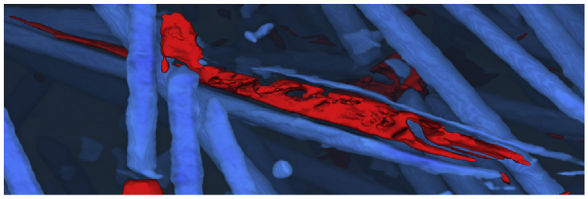

(f) $\varepsilon_6 = 5.3\%$, $\sigma_6 = 74.1$ MPa

Fig. 10. Example of a fibre failure transversally to tensile loading direction (tensile direction is vertical).

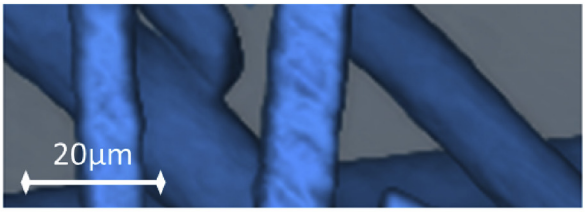

(a) $\varepsilon_2 = 1.1\%$, $\sigma_2 = 28.0$ MPa, $\sigma_{MT}^{local} = 168.0$ MPa

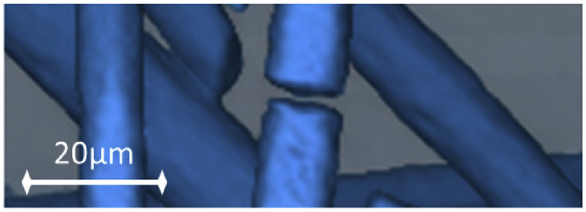

(b) $\varepsilon_3 = 2.1\%$, $\sigma_3 = 49.7$ MPa, $\sigma_{MT}^{local} = 291.1$ MPa

Fig. 11. Local stress thresholds to break (tensile direction is vertical).

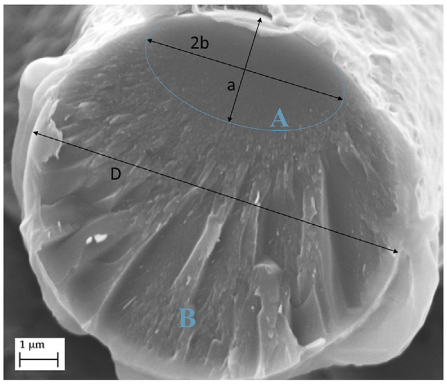

(a) SEM Fractography on a broken fibre

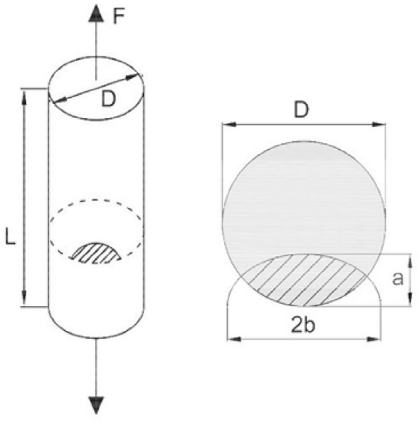

(b) Geometry to evaluate critical stress intensity factors

Fig. 12. Broken fibre under tensile stress (tensile direction is vertical).

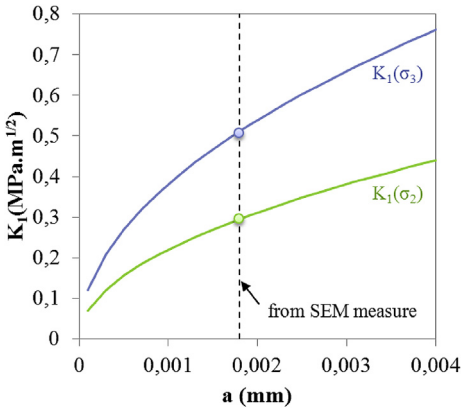

Fig. 13. Framing values following initial notched fibre geometry and microscopic stress estimations.

($K_{1C}^{E-glass} = 0.6$ MPa.$m^{1/2}$). Two possible reasons for such mismatch can be considered. The first one is the possible K_{1C} heterogeneity at that scale along the fibre. The second one is the local overstress compared to the Mori-Tanaka's scheme. This local overstress is supposed, due to systematic observation of close fibres with different orientation in the neighbourhood of fibre failures. Ongoing finite elements computation on real microstructures will allow to answer more accurately these aspects.

3.2.4. Damage growth in the matrix

This mechanism refers to the growth of damage markers in the bulk of polymer matrix. The scenario leading to these markers seems to be the same in the whole observed volume: the initiation phase is driven either by damage at fibre ends or a zone of confined matrix between two fibres with significant differences in orientations. Both situations result in a stress concentration and drive toward damage appearance and growth as seen in Fig. 14. This

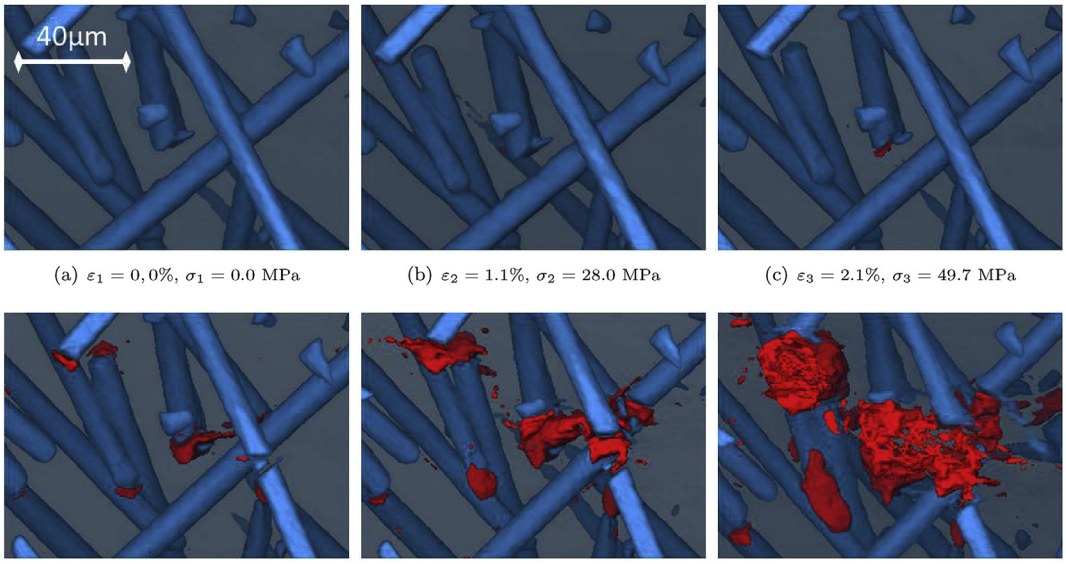

(a) $\varepsilon_1 = 0,0\%$, $\sigma_1 = 0.0$ MPa (b) $\varepsilon_2 = 1.1\%$, $\sigma_2 = 28.0$ MPa (c) $\varepsilon_3 = 2.1\%$, $\sigma_3 = 49.7$ MPa

(d) $\varepsilon_4 = 3.2\%$, $\sigma_4 = 63.9$ MPa (e) $\varepsilon_5 = 4.2\%$, $\sigma_5 = 71.6$ MPa (f) $\varepsilon_6 = 5.3\%$, $\sigma_6 = 74.1$ MPa

Fig. 14. Damage in the matrix, initiated by fibres failures (tensile direction is vertical).

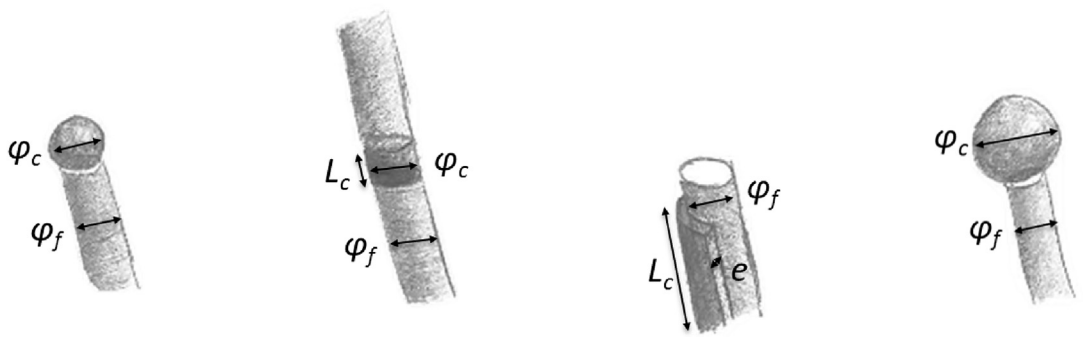

(a) Fibre end damage $\phi_{cavity} \approx \phi_{fibre}$ (b) Fibre failure $\phi_{cavity} \approx \phi_{fibre}$ (c) Debonding $L_{cavity} > e$ (d) Damage growth $\phi_{cavity} > \phi_{fibre}$

Fig. 15. Geometry associated with thresholds for damage markers morphology.

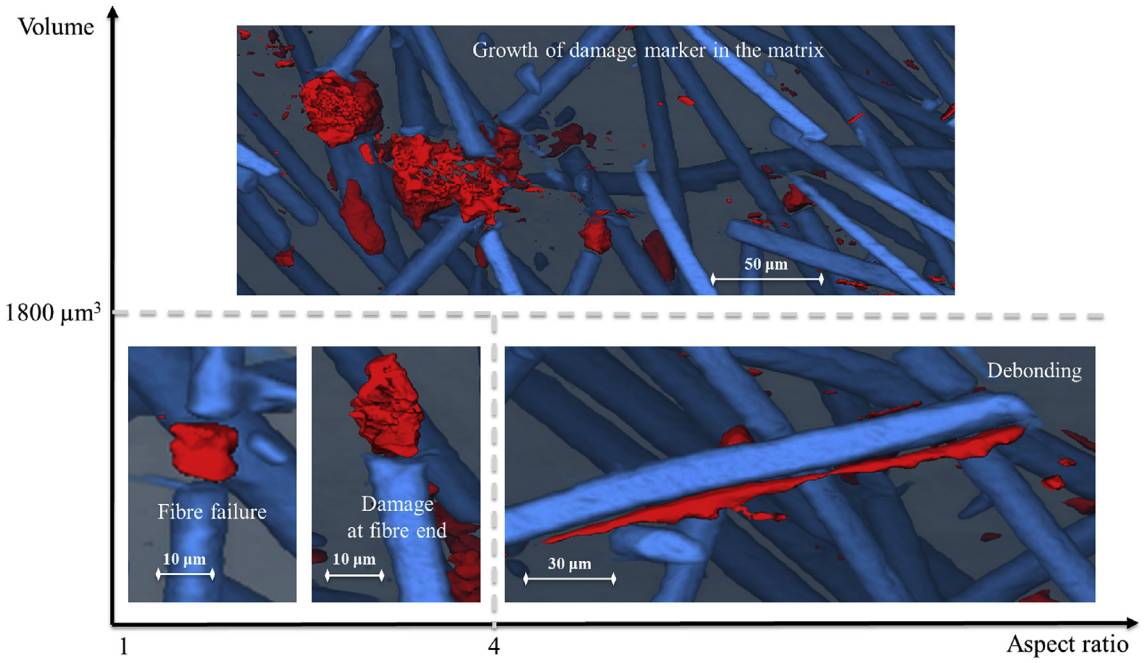

Fig. 16. Mechanisms distribution according to defined morphological thresholds.

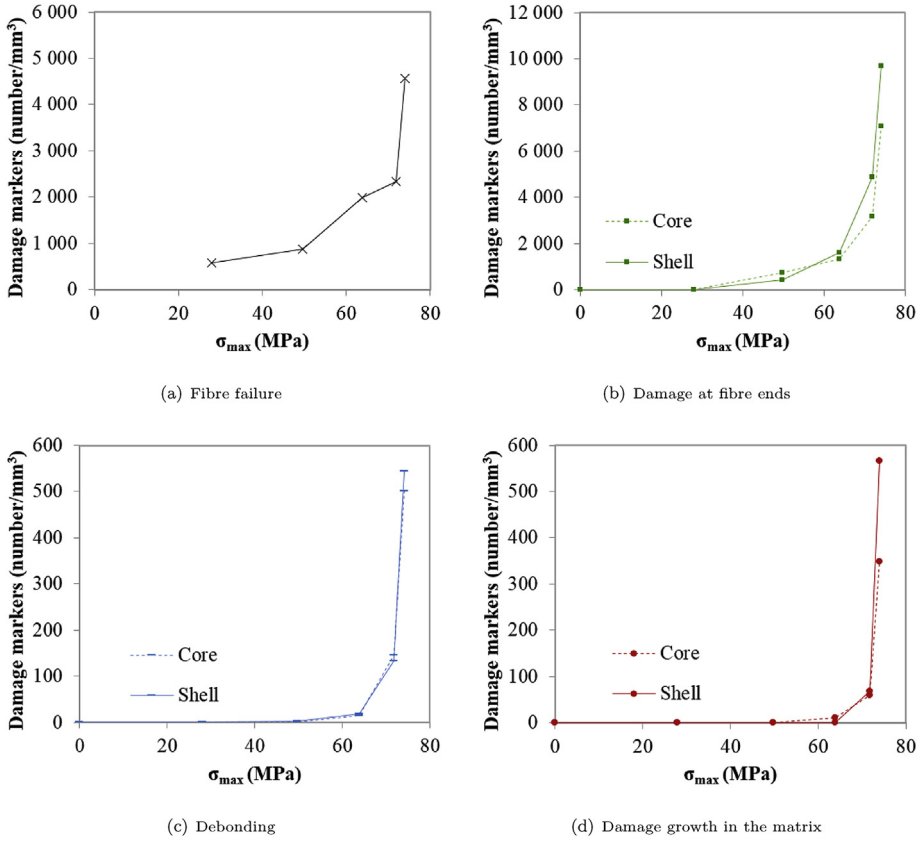

(a) Fibre failure

(b) Damage at fibre ends

(c) Debonding

(d) Damage growth in the matrix

Fig. 17. Core and shell damage mechanisms kinetics during tensile test.

damage development in the bulk of polymer matrix grows in a spherical way and is not aligned with the macroscopic stress direction, probably due to stress triaxiality. The markers can then reach large volumes, as shown in Fig. 14(f).

3.3. Damage mechanisms and geometry of markers

Observed damage mechanisms have been qualitatively described, but several thousands of damage markers are detected

Table 2
Values C_{ij} to calculate the local stress intensity factor K_1 [21].

C_{ij}	j = 0	j = 1	j = 2	j = 3
I = 0	1.118	−0.171	−0.339	0.130
I = 2	1.405	5.902	−9.057	3.032
I = 3	3.891	−20.370	23.217	−7.555
I = 4	8.328	21.895	−36.992	12.676

throughout the overall investigated volumes. It has been noticed that as a function of the stress level, morphology (i.e. geometrical features) of damage markers evolves. In order to propose efficient quantitative analyses of the microtomographic data, damage markers have been studied considering their morphology and orientation with respect to macroscopic tensile direction.

For each previously identified mechanism, representative damage markers have been described by their length, volume and aspect ratio. The fibre diameter (10.9 μm in this study) is taken as a reference length. Damage at fibre ends, non-distinguishable from fibre failure, is characterized by medium volume (equivalent to the volume of a sphere with the diameter of the fibre cf. Fig. 15(a) and (b)). Debonding corresponds to damage markers with high aspect ratio, as seen in Fig. 15(c). Damage markers corresponding to damage growth in the matrix have important volumes (see Fig. 15(d)) and tend to be spherical (aspect ratio close to 1), they correspond to ductility development in the material.

From this description, it is possible to define specific thresholds to consistently associate each damage marker to a given mechanism. Aspect ratio is considered high when its value is superior to 4, meaning damage markers with a length at least four times superior than their width. The volumetric threshold to discriminate large damage markers from medium ones is set to the volume of a sphere having 1.5 times the diameter of fibre: $\phi_{marker} = 1.5\phi_{fibre}$, that being 1800 μm^3 in the case of the study. Damage markers identified after image processing are therefore classified following these thresholds as illustrated by Fig. 16. Note that damage markers with large volume and high aspect ratio are rare. Such voids will be considered as resulting from the coalescence of other damage, and so, as a form of damage growth.

3.4. Damage mechanisms analysis at the specimen scale

Damage markers populations have been analysed depending on their mechanism and their position in the thickness (core or shell).

3.4.1. Evolution of density, volume and orientation of damage markers population

The analysis concerns the largest volume common to all observed volumes so that exactly the same microstructures were considered. It results in a cube of 840 μm edge size. For this part of the specimen, around 9,000 fibres per mm^3 have been identified plus 1,000 damage markers per mm^3 for the first step and over 10,000 damage markers per mm^3 for the final step. In the first acquisition (initial state), there already are few damage markers. Some of these initial defects are existing cavities due to the process, but most of them result from artefact (markers located on the rotation axis and on centred rings). This defect population has been removed from the data for the following quantitative study (concerned 1/10 of the final markers density).

The density of damage markers for each mechanism has been evaluated and represented in Fig. 17 as a function of macroscopic stress level. There is a continuous increase of the global number of damage markers. The population of damage markers at fibre ends is getting bigger during the test, in the same proportions as fibre failures. The density of these two mechanisms prevails over densities of others: they are spread in the whole gage length. It is remarkable that in average at the end of the test, almost all fibres exhibit damage at their ends and one fibre over two is broken. The later remark is particularly important since, as previously said, this mechanism is rarely reported in the literature to that extent.

Concerning the debonding, its detection is belated (only visible from the fourth step $\sigma_4 = 63.9$ MPa), but its density then increases quickly. A similar assessment is made about speed of expansion for damage growth in the matrix: the density is stable until last step of the tensile test, when density soars.

The evolution of the damage volume is significant of the stress increase, as observed in diagrams from Fig. 18. In both shell and core sections, there are the same proportions of damage hold in less than 0.05% of the volume until 60 MPa and then an expansion reaching a volumetric fraction of 0.2%.

The evolution of the mean volume of damage markers according to their orientation with respect to the tensile direction (0°), at each step of the test and per damage mechanism, are presented in Fig. 19. For each step, the population of damage markers is split between shell and core. Orientation of damage markers at fibre ends (Fig. 19(b)) is similar to fibres direction for early and middle steps and spreads toward the tensile direction before failure of the specimen. When detected at the final steps of the test, markers for debonding have a range of preferential orientations between fibres orientation (45°) and 90° (cf. Fig. 19(c)). This orientation range can be explained by the combination of the development of fibre-matrix interface damage driven by the normal and shear stresses acting at the interface (as expressed in some micro-mechanical models such as in Refs. [23,24]), together with an heterogeneous distribution of fibre orientation in that range. In the case of damage growth in the matrix, the orientation of markers is rather perpendicular to the macroscopic tensile direction for early steps and spreads toward all directions with the stress increase. This observation is coherent with the fact that this category of damage markers tend to be spherical.

3.4.2. Core–shell effect

Evolutions of damage markers populations are close for the shell and for the core, but some differences exist with specificities to each damage mechanism.

The volume of markers corresponding to damage at fibre ends is lower in the core than in the shell (cf. Fig. 18(a)). Actually, this slight difference is coherent with differences of fibres density and fibres orientation dispersion between core and shell, previously described in the paragraph 2.3. This is mostly due to the scattered orientation centred on 63° of the core fibres, that is less favourable to initiate that damage type (illustrated in Fig. 19(a)). Those differences are evidenced in Fig. 20 that illustrates the projection of damage markers through the gage length at different stages of the test. This projection is made in the plane normal to the tensile direction, in two different zones of the gage length (see Fig. 21). Debonding, on the other hand, is promoted in the core (see Figs. 17(c) and 18(c)) due to a more favourable orientation of the fibre-matrix interface and a slightly higher density of fibres in that zone (17% fibres in volume in the core against 11% in the shell). In addition, it should be noticed that despite different main fibre orientations between the core and the shell, the debonding damage markers orientation is the same. This clearly indicates that debonding is a stress driven process. Finally, the evolution of damage markers location is correlated to the fracture surface where two failure modes can be distinguished. The first one is typical of a ductile fracture while the second one is typical of a brittle fracture. The two different modes are indicated in Fig. 21 with the fracture initiation in the core region. The projected damage evolution given in Fig. 20 for the two failure modes (zone 1: ductile, zone 2 brittle)

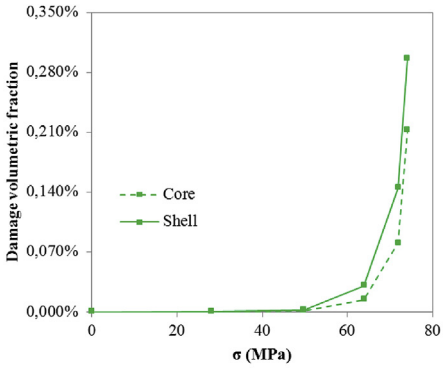

(a) Damage at fibre ends

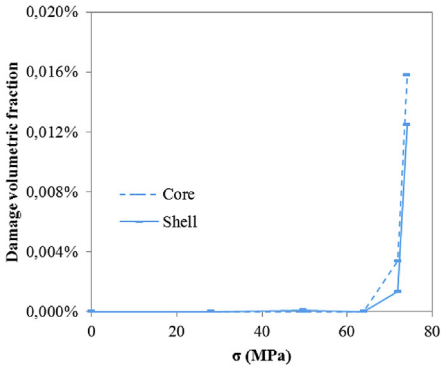

(b) Debonding

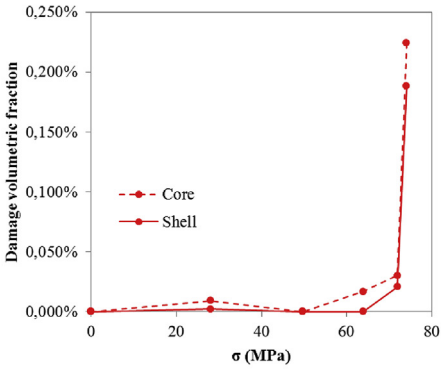

(c) Damage growth in the matrix

Fig. 18. Volumetric fraction evolution of damage during tensile test in core and shell.

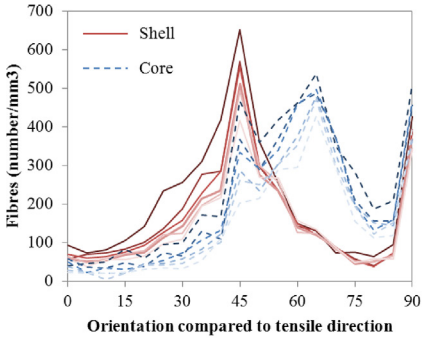

(a) Fibres orientation

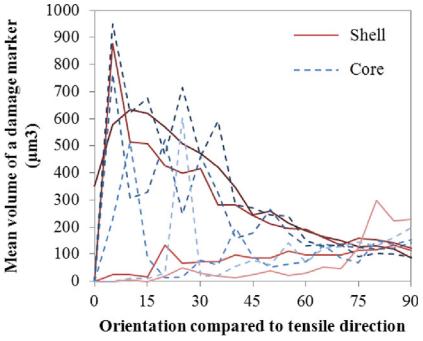

(b) Damage at fibre ends orientation

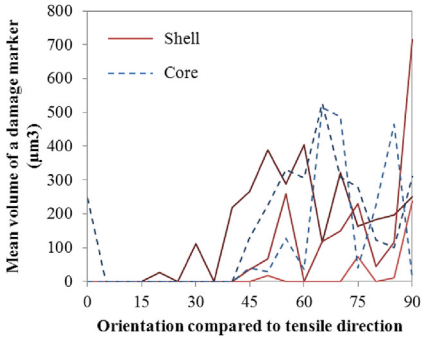

(c) Debonding orientation

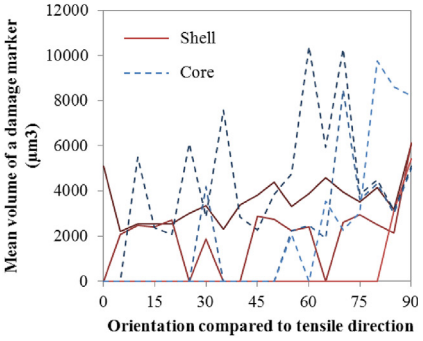

(d) Damage growth in the matrix orientation

Fig. 19. Evolution of damage markers during tensile test as a function of their orientation.

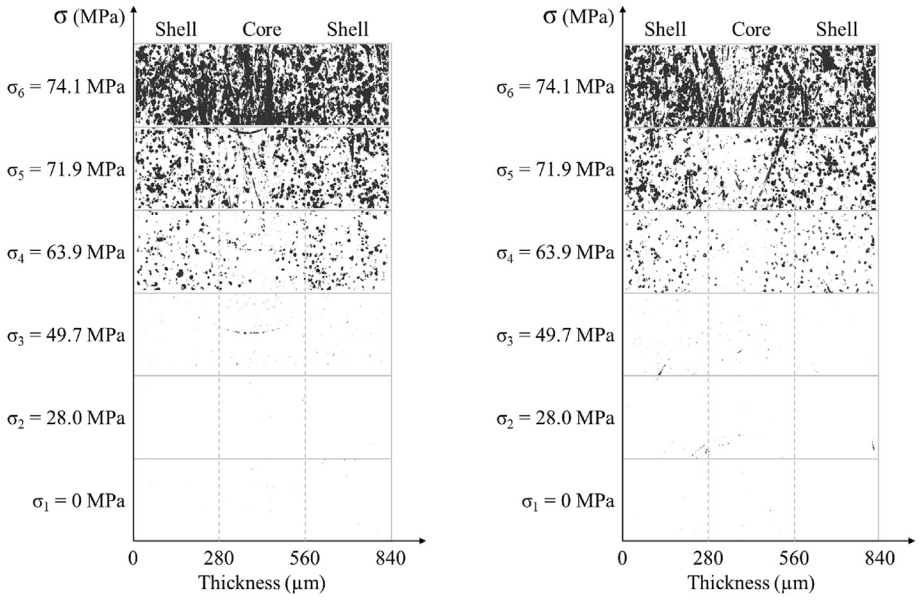

Fig. 20. Evolution of the damage during tensile test for two different zones of the fracture surface, presented in Fig. 21.

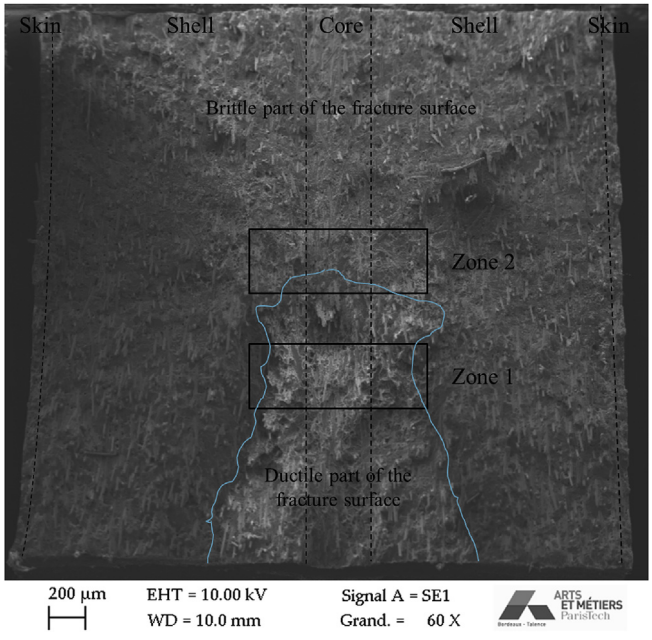

Fig. 21. SEM observation of the fracture surface of the specimen.

indicates that the differentiation between the two happens in the very last stage. It also appears that the debonding in the core region seems to play a significant role in the percolation of damage.

3.5. Damage scenario

During the first steps of the tensile test, the stress rise causes an increase of the number of damage markers. Fibre failure and damage at fibre ends are there the predominant mechanisms, spread in the whole gage length. When 2/3 of the ultimate stress is reached, a new mechanism is detected: debonding appears at the fibre-matrix interface. In parallel, other damage markers are growing in the matrix: from initial defects, damage at fibre ends or fibre failures. Through the test, the stress field is redistributed with the microstructural evolution: after a fibre failure, surrounding matrix has to bear this overstress, besides defects and deformation. Important damage markers are linked with high deformation of the matrix, load bearing transfer from fibres to the matrix. Until the final step of the test, volumes dedicated to each damage mechanism soar. There is coalescence between damage markers with a very probable important role of the debonding.

4. Conclusion

In this work, an experimental procedure and a computed microtomography data post-processing methodology were developed in order to distinguish and quantify the different damage mechanisms occurring in short fibre reinforced polymers. The proposed approach allows to reach quantitatively the evolution of a population of more than 20,000 damage markers that ensure the representativeness of the experimental data compared to already published works. It also allows to differentiate particular zones, such as the core and shell zones in the thickness of injected specimens. The following conclusions can be drawn:

- Four main mechanisms are identified: fibre failure, damage at fibre ends, debonding, matrix damage. The four mechanisms, largely spread in the overall analysed volume, are found to evolve differently as a function of the applied stress and the spatial location in the specimen. Despite not well reported in the literature, fibre failure appears as a major damage mechanism. This mechanism concerns two thirds of the initial fibre population (it is the second main mechanism observed with fibre-end damage) and evolves continuously up to failure. Damage growth in the matrix appears as a consequence of fibre failure and damage at fibre ends, which appears at medium stress ranges due to weak interface properties. Debonding appears in the last stage and seems to play an important role in the damage percolation at the specimen scale.

- As expected, local fibre orientation has a key role on the development of damage at fibre ends and debonding. However the orientation of those damage markers does not coincide with the orientation distribution of fibres, but results from a combination of this distribution with the local stress field. The obtained data will allow a direct identification of an interfacial model as used in micromechanical approaches. Local fibre orientation plays a key role in the final failure process (damage percolation role of debonding at the specimen scale).
- Most of the above mentioned damage mechanisms are found to be triggered by local confinement, due to fibres in close vicinity and/or fibre crossing that induces local overstress. The degree of fibre misalignment is a key parameter to control for those materials.
- The proposed analysis allows to differentiate the damage evolution in the core and the shell parts of the specimen. In particular, it is possible to correlate the location of the failure initiation with the local evolution of 3D damage. The core–shell structure of the specimen does impact the final failure mode by promoting debonding in the core due to local critical microstructure configuration. Despite the relatively small contribution of the core zone on the macroscopic mechanical behaviour (considering the shell/core volume ratio), it plays a key role in the final failure and such on the macroscopic failure properties. Finally it should be noticed that a more pronounced effect is expected for other specimens orientations (0°, 90°, etc).

This methodology will allow to directly identify (not by inverse method) the damage parameters classically used in micromechanical models. As this analysis is strongly linked with microstructure orientation and matrix behaviour (temperature and conditioning dependent), the ongoing work includes similar analysis for different specimen orientations and conditioning.

Acknowledgement

The authors gratefully acknowledge Solvay Engineering Plastics for supporting this work and for providing specimens. This work was performed in the framework of the DURAFIP project (FUI project supported by Oseo).

References

[1] Fu S-Y, Lauke B. Effects of fiber length and fiber orientation distributions on the tensile strength of short-fiber-reinforced polymers. Compos Sci Technol 1996;56:1179–90.
[2] Bernasconi A, Cosmi F, Hine PJ. Analysis of fibre orientation distribution in short fibre reinforced polymers: a comparison between optical and tomographic methods. Compos Sci Technol 2012;72(16):2002–8.
[3] Thomason JL. The influence of fibre properties on the performance of glass-fibre-reinforced polyamide 6,6. Compos Sci Technol 1999;59:2315–28.
[4] Thomason JL. The influence of fibre length, diameter and concentration on the modulus of glass fibre reinforced polyamide 6,6. Compos Part A 2008;39:1732–8.
[5] Horst JJ, Spoormaker JL. Mechanisms of fatigue in short glass fiber reinforced polyamide 6. Polym Eng Sci 1996;36(22):2718–26.
[6] Sato N, Kurauchi T, Sato S, Kamigaito O. Mechanism of fracture of short glass fibre-reinforced polyamide thermoplastic. J Mater Sci 1984;19:1145–52.
[7] Sato N, Kurauchi T, Sato S, Kamigaito O. Microfailure behaviour of randomly dispersed short fibre reinforced thermoplastic composites obtained by direct SEM observation. J Mater Sci 1991;26:3891–8.
[8] Buffiere J-Y, Maire E, Cloetens P, Peix G, Salome M, Baruchel J. In situ damage assessment in microheterogeneous material using high resolution x-ray tomography. ESFR Newsl 1998;30:20–1.
[9] Salvo L, Cloetens P, Maire E, Zabler S, Blandin JJ, Buffiere J-Y, et al. X-ray micro-tomography an attractive characterisation technique in materials science. Nucl Instrum Methods Phys Res B 2003;200:273–86.
[10] Arif MF, Saintier N, Meraghni F, Fitoussi J, Chemisky Y, Robert G. Multiscale fatigue damage characterization in short glass fiber reinforced polyamide-66. Compos Part B 2014;61:55–65.
[11] Kak A, Slaney M. Principles of computerized tomographic imaging. New York: IEEE; 1988.
[12] Valentin D, Paray F, Guetta B. The hygrothermal behaviour of glass fibre reinforced pa66 composites: a study of the effect of water absorption on their mechanical properties. J Mater Sci 1987;22:46–56.
[13] Barbouchi S, Bellenger V, Tcharkhtchi A, Castaing Ph, Jollivet T. Effect of water on the fatigue behaviour of a pa66/glass fibers composite material. J Mater Sci 2007;42(6):2181–8.
[14] Arif MF, Meraghni F, Chemisky Y, Despringre N, Robert G. In situ damage mechanisms investigation of pa66gf30 composite: effect of relative humidity. Compos Part B 2014;58:487–95.
[15] Bernasconi A, Cosmi F, Dreossi D. Local anisotropy analysis of injection moulded fibre reinforced polymer composites. Compos Sci Technol 2008;68:2574–81.
[16] Horst JJ, Spoormaker JL. Fatigue fracture mechanisms and fractography of short-glassfibre-reinforced polyamide 6. J Mater Sci 1997;32(14):3641–51.
[17] Horst JJ, Salienko NV, Spoormaker JL. Fibre-matrix debonding stress analysis for short fibre-reinforced materials with matrix plasticity, finite element modelling and experimental verification. Compos Part A 1998;29:525–31.
[18] Klimkeit B, Castagnet S, Nadot Y, El Habib A, Benoit G, Bergamo S, et al. Fatigue damage mechanisms in short fiber reinforced PBT+PET GF30. Mater Sci Eng A 2011;528(3):1577–88.
[19] Mori T, Tanaka K. Average stress in matrix and average elastic energy of materials with misfitting inclusions. Acta Metall 1973;21:571–4.
[20] Ilankeeran PK, Mohite PM, Kamle S. Axial tensile testing of single fibres. Mod Mech Eng 2012;2:151–6.
[21] Toribio J, Ayaso J, González B, Matos J-C, Vergara D. Critical stress intensity factors in steel cracked wires. In: 3rd International Conference on Integrity, Reliability and Failure; 2009.
[22] Astiz MA. An incompatible singular elastic element for two- and three-dimensional crack problems. Int J Fract 1986;31:105–24.
[23] Fitoussi J, Guo G, Baptiste D. A statistical micromechanical model of anisotropic damage for S.M.C. composites. Compos Sci Technol 1998;58(5):759–63.
[24] Jendli Z, Meraghni F, Fitoussi J, Baptiste D. Micromechanical analysis of strain rate effect on damage evolution in sheet molding compound composites. Compos Part A Appl Sci Manuf 2004;35(7–8):779–85.